Sub-Nyquist Sampling and Fourier Domain Beamforming in Volumetric Ultrasound Imaging

Amir Burshtein, Michael Birk, Tanya Chernyakova, *Student Member, IEEE*, Alon Eilam, Arcady Kempinski, and Yonina C. Eldar, *Fellow, IEEE*

Abstract—A key step in ultrasound image formation is digital beamforming of signals sampled by several transducer elements placed upon an array. High-resolution digital beamforming introduces the demand for sampling rates significantly higher than the signals' Nyquist rate, which greatly increases the volume of data that must be transmitted from the system's front end. In 3-D ultrasound imaging, 2-D transducer arrays rather than 1-D arrays are used, and more scan lines are needed. This implies that the amount of sampled data is vastly increased with respect to 2-D imaging. In this work, we show that a considerable reduction in data rate can be achieved by applying the ideas of Xampling and frequency domain beamforming (FDBF), leading to a sub-Nyquist sampling rate, which uses only a portion of the bandwidth of the ultrasound signals to reconstruct the image. We extend previous work on FDBF for 2-D ultrasound imaging to accommodate the geometry imposed by volumetric scanning and a 2-D grid of transducer elements. High image quality from low-rate samples is demonstrated by simulation of a phantom image composed of several small reflectors. Our technique is then applied to raw data of a heart ventricle phantom obtained by a commercial 3-D ultrasound system. We show that by performing 3-D beamforming in the frequency domain, sub-Nyquist sampling and low processing rate are achievable, while maintaining adequate image quality.

Index Terms—Array processing, beamforming, compressed sensing (CS), ultrasound.

I. Introduction

SONOGRAPHY is one the most widely used imaging modalities due to its relative simplicity and radiation-free operation. It uses multiple transducer elements for tissue visualization by radiating it with acoustic energy. The image is typically composed of multiple scanlines, obtained by sequential insonification of the medium using focused acoustic beams. Reflected signals detected at each transducer element are sampled prior to digital processing. Beamforming is a key step in image formation, generating receive sensitivity profiles focused at any desired point within the image (2-D) or volume (3-D). The resulting beamformed signal, characterized by enhanced signal-to-noise ratio (SNR) and improved angular localization, forms a line in the image, which we refer to as beam.

The aforementioned approach, used by most commercial systems today, is characterized by two important parameters: sampling and processing rate, and frame or volume rate. Sampling rates required to perform high-resolution digital beamforming are significantly higher than the Nyquist rate of the signal [1]. Taking into account the number of transducer elements and the number of lines in an image, the amount of sampled data that need to be transferred to the processing unit and digitally processed is enormous, even in 2-D imaging setups. This motivates methods for sampling rate reduction. In addition, regardless of computational power, the frame/volume rate in this approach is limited by the time required to transmit a beam, to receive and process the resulting echoes, and to repeat the process for all image lines.

Among the focus areas, the main focus area in the study of ultrasonic scanning is the development of real-time 3-D ultrasound imaging, which overcomes major constraints of 2-D imaging. 3-D volume acquisition eliminates operator dependence in the imaging process: once the 3-D data set is obtained, any plane within it is available for visualization by appropriate cropping and slicing. In addition, a variety of parameters can be measured from a 3-D image in a more accurate and reproducible way compared to 2-D imaging [2], [3], [4]. Finally, many anatomical structures, e.g., the mitral valve, are intrinsically 3-D [5], implying that their complex anatomy cannot be captured efficiently with 2-D techniques.

A straight forward approach to 3-D volume acquisition is to use a mechanically rotating 1-D probe [6]. However, this results in extremely low volume rates, leading to unacceptable motion artifacts in echocardiography applications. Fully sampled 2-D arrays, an extension of the 1-D array to both lateral and elevation directions, are the most advanced technology for intrinsic 3-D acquisition. Such arrays allow for significant improvement in frame rate and real-time capabilities. This is obtained by parallel processing, namely, electronically receiving data from several points in both lateral and elevation dimensions within the 3-D volume simultaneously [7], [8].

Despite the high frame rate, angular resolution, and SNR, fully sampled 2-D arrays pose several engineering challenges [2], [9]. Due to the significantly increased number of elements, which can be as high as several thousand, the main difficulty from a hardware perspective is connecting the elements to electronic channels. In addition, the amounts of sampled data, acquired at each transmission, create a bottleneck at the data transfer step and pose a severe computational burden on the digital signal processing hardware. To avoid large connecting cables, leading to unacceptable probe size and weight, and to reduce power and size, as well as data rates, several techniques for element number reduction have been proposed.

A. Related Work

In a sparse aperture, only a subset of the 2-D grid of elements is used upon reception and/or transmission. Several studies investigate strategies for optimal subset choices [8]–[14] which limit the degradation in image quality due to energy loss and high grating and sidelobes. In [15], Savord and Solomon present a subarray beamforming approach allowing for significant reduction in the number of channels by suboptimal analog beamforming, also referred to as microbeamforming. This method has been implemented in leading commercial systems. Another promising method, synthetic aperture, was adopted from sonar processing and geological applications [16], [17]. This approach exploits multiplexing to control a fully sampled 2-D array with a small number of electronic channels. Although providing improved image quality, synthetic aperture suffers from reduced frame rate and huge amounts of sampled data. The concept of separable beamforming proposed in [18] and [19] allows for computationally efficient implementation of 2-D beamforming by splitting it into two separable 1-D steps. However, the overall amount of data remains the same since all the transducer elements are sampled.

Even when the number of elements is reduced, the amount of sampled data is still very large due to the high number of scan lines. Consider imaging of a 3-D volume, using K scan lines in each one of K 2-D cross sections of the volume. Scanning the entire volume yields a total of $K \times K$ scan lines. To maintain the angular resolution in each one of the K cross sections in the 3-D frame in comparison to 2-D ultrasound imaging, one is forced to essentially quadrate the amount of data with respect to 2-D imaging, given the same number of transducers. Lorintiu *et al.* propose to skip the acquisition of up to 80% of image lines and then recover the missing data using a sparse representation of the ultrasound volume in learned overcomplete dictionaries [20], [21]. This work, however, does not address the number of elements involved in acquisition of each one of the obtained scanlines.

In 2-D imaging, a number of strategies for data rate reduction have been proposed, which exploit signal structure and rely on compressed sensing (CS) techniques [22], [23]. Most of the proposed methods can be divided into two categories. The first allows for sampling and recovery of each individual detected signal at a low rate assuming sufficiently high SNR [24]–[27]. The second deals with recovering a beamformed signal from its low-rate samples [28]–[30] assuming that one has access to the continuous-time beamformed data. In practice, the beamformed signal is formed digitally at a high rate from samples of each of the individual received signals.

A practical method to acquire low-rate beamformed data from low-rate samples of the received signals is reported in [31]. An entire framework enabling compressed ultrasound imaging in 2-D, including sub-Nyquist data acquisition from each transducer element, low-rate processing, and beamformed signal reconstruction is proposed in [32]. This approach is based on beamforming in the frequency domain. Specifically, the Fourier coefficients of the beam are computed as a linear combination of those of the individual detected signals, obtained from their low-rate samples. When all the beam's Fourier coefficients within its bandwidth are computed, the sampling and processing rates are equal to the effective Nyquist rate. The beam in time is then recovered by an inverse Fourier transform. When further rate reduction is required, only a subset of the beam's Fourier coefficients is obtained, which is equivalent to sub-Nyquist sampling. Recovery then relies on an appropriate model of the beam, that compensates for the lack of frequency data, and optimization methods. Low-rate data acquisition is based on the ideas of Xampling [24]–[34], which obtains the Fourier coefficients of individual detected signals from their low-rate samples.

B. Contributions

In this work, we generalize beamforming in frequency developed for 2-D imaging [31], [32] to 3-D imaging, to enable data rate reduction. Our approach can be applied in conjunction with any of the existing methods for element or image line reduction.

In 3-D imaging, the same low-rate sampling scheme can be applied to the individual signals detected at the elements of the 2-D transducer, leading to considerable rate reduction, as elaborated on in Section III-B. However, to benefit from the rate reduction, 3-D beamforming must be performed in frequency similarly to the 2-D setup. We prove that the relationship between the beam and the detected signals in the frequency domain, the core of beamforming in frequency, holds for 3-D imaging as well.

We then derive a frequency domain formulation of beamforming that accounts for the 2-D geometry of the transducer array and the 3-D geometry of the medium. We show that 3-D frequency domain beamforming (FDBF) can be implemented efficiently due to the decay property of the distortion function translating the dynamic beamforming time delays into the frequency domain. When sub-Nyquist sampling and processing are applied, signal structure needs to be exploited to recover the beam from the sub-Nyquist set of its Fourier coefficients. To this end we prove that a 3-D beamformed signal obeys a finite rate of innovation (FRI) [22] model, just as in 2-D.

We demonstrate our results through simulations and experiments and examine the performance of 3-D FDBF in terms of the lateral point spread function (LPSF), axial point spread function (APSF), and SNR. We next evaluate the effect of channel rate reduction, an alternative approach to reduce the number of samples, on image quality. Such a reduction is not required in 2-D imaging since the number of transducer elements is relatively small. However, in 3-D imaging with 2-D arrays, such a reduction is often unavoidable due to hardware limitations. Reducing the amount of transducer elements enhances noise levels in the image and deteriorates the lateral resolution, while our technique mainly affects the axial resolution. We conclude that when the element number reduction is unavoidable, incorporation of 3-D FDBF does not cause further degradation in lateral resolution and SNR, while providing additional data rate reduction. Finally, we incorporate our approach into a commercial imaging system performing subarray beamforming. In this setup, the element reduction and 3-D FDBF are applied in conjunction. The results show that rate reduction obtained by 3-D FDBF does not introduce further image quality degradation.
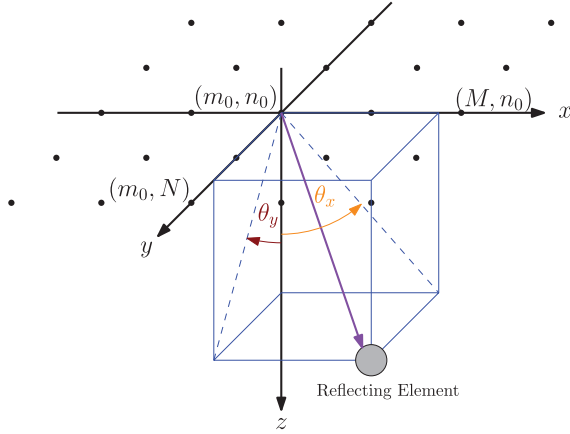
Fig. 1. $M \times N$ transducers placed in the x–y plane. An acoustic pulse is transmitted in a direction θ_x, θ_y. The echoes scattered from perturbations in the radiated tissue are received by the array elements.

We note that 3-D frequency-domain dynamic beamforming based on the 2-D fast Fourier transform (FFT) was proposed for sonar systems back in the 1990s [35]. This approach, however, relies on the assumption that the signals used for insonification are narrow band. This is true for sonar, where the bandwidth is two orders of magnitude smaller than the central frequency. In medical imaging, the central frequency is approximately equal to the bandwidth, so that this approach is inapplicable.

This paper is organized as follows. In Section II, we review standard time-domain processing for a 3-D imaging setup. In Sections III and IV, we describe the principles of 3-D FDBF, image reconstruction, and achieved rate reduction. Simulation results and experiments are presented in Section V. Section VI concludes this paper.

II. IMPLEMENTATION OF BEAMFORMING IN TIME

Beamforming is a common signal-processing technique that enables spatial selectivity of signal transmission or reception [36]. In ultrasound imaging, it allows for SNR and lateral resolution improvement. Modern imaging systems transmit and receive acoustic pulses using multiple transducer elements. These elements comprise an array, generating a transmitted beam which is steered spatially by applying appropriate time delays to each element. The transducer receives acoustic pulses scattered by tissue structures, which are then sampled and processed digitally to reconstruct an image line. Reconstruction is performed with a technique known as dynamic beamforming, where image quality is enhanced by summing the signals at individual elements after their alignment by appropriate time delays.

To derive our frequency-domain implementation of 3-D beamforming, we begin by introducing standard time-domain processing. Consider a grid of $M \times N$ transducers located in the x–y plane, as depicted in Fig. 1. The geometry imposed by 3-D ultrasound imaging requires the use of two steering angles and thus a 2-D array of transducers. The entire grid transmits pulses into the tissue. We note that the grid may have a small curvature along the z-axis, so the array elements do not lie in the same plane. For the sake of simplicity, this type of curvature is not displayed in Fig. 1.

We choose a reference element (m_0, n_0) placed at the origin, and denote the distances along the x- and y-axes to the (m, n) element by δ_m, δ_n, respectively. We also denote the height of the (m, n) element with respect to the origin by $\delta_{m,n}^z$ for the case where there exists a curvature along the z-axis. Note that we assume $\delta_{m_0,n_0}^z = 0$, so that the reference element is not necessarily included in the transducer grid and is defined for mathematical convenience. Let us consider a pulse transmitted along a scan line specified by spatial angles θ_x, θ_y. Setting $t = 0$ at the moment of transmission from the (m_0, n_0) element, it can be shown that at time $t \geq 0$ the pulse reaches the coordinates

$$(x(t), y(t), z(t)) = ct(x_\theta, y_\theta, z_\theta) \tag{1}$$

with

$$
\begin{aligned}
x_\theta &= \frac{\sin \theta_x \cos \theta_y}{\sqrt{1 - \sin^2 \theta_x \sin^2 \theta_y}} \\
y_\theta &= \frac{\cos \theta_x \sin \theta_y}{\sqrt{1 - \sin^2 \theta_x \sin^2 \theta_y}} \\
z_\theta &= \frac{\cos \theta_x \cos \theta_y}{\sqrt{1 - \sin^2 \theta_x \sin^2 \theta_y}}.
\end{aligned}
\tag{2}
$$

Here, c is the propagation velocity in the medium. A point reflector located at this position scatters the energy, such that the echo is detected by all array elements at a time depending on their locations.

Denote by $\varphi_{m,n}(t; \theta_x, \theta_y)$ the signal detected by the (m, n) element and by $\hat{\tau}_{m,n}(t; \theta_x, \theta_y)$ the time of detection. Then,

$$\hat{\tau}_{m,n}(t; \theta_x, \theta_y) = t + \frac{d_{m,n}(t; \theta_x, \theta_y)}{c} \tag{3}$$

where

$$
d_{m,n}(t; \theta_x, \theta_y) = \\
\sqrt{(x(t) - \delta_m)^2 + (y(t) - \delta_n)^2 + (z(t) - \delta_{m,n}^z)^2} \tag{4}
$$

is the distance traveled by the reflection. Beamforming involves summing the signals detected by multiple receivers while compensating for the differences in detection time.

Using (3), the detection time at (m_0, n_0) is $\hat{\tau}_{m_0,n_0}(t; \theta_x, \theta_y) = 2t$ since $\delta_{m_0} = \delta_{n_0} = \delta_{m,n}^z = 0$. We wish to apply a delay to $\varphi_{m,n}(t; \theta_x, \theta_y)$ such that the resulting signal, denoted by $\hat{\varphi}_{m,n}(t; \theta_x, \theta_y)$, satisfies

$$\hat{\varphi}_{m,n}(2t; \theta_x, \theta_y) = \varphi_{m,n}(\hat{\tau}_{m,n}(t; \theta_x, \theta_y); \theta_x, \theta_y).$$

Doing so, we can align the reflection detected by the (m, n) receiver with the one detected at (m_0, n_0). Denoting $\tau_{m,n}(t; \theta_x, \theta_y) = \hat{\tau}_{m,n}(t/2; \theta_x, \theta_y)$ and using (3), the following aligned signal is obtained:

$$
\begin{aligned}
&\hat{\varphi}_{m,n}(t; \theta_x, \theta_y) = \varphi_{m,n}(\tau_{m,n}(t; \theta_x, \theta_y); \theta_x, \theta_y) \\
&\tau_{m,n}(t; \theta_x, \theta_y) = \\
&\frac{1}{2} \left(t + \sqrt{t^2 + 4|\gamma_{m,n}|^2 - 4t\left(\gamma_m x_\theta + \gamma_n y_\theta + \gamma_{m,n}^z z_\theta\right)} \right)
\end{aligned}
\tag{5}
$$

where we defined $\gamma_m = \delta_m/c$, $\gamma_n = \delta_n/c$, $\gamma_{m,n}^z = \delta_{m,n}^z/c$, and $|\gamma_{m,n}| = \sqrt{\gamma_m^2 + \gamma_n^2 + (\gamma_{m,n}^z)^2}$.

The beamformed signal may now be derived by averaging the aligned signals. We assume that the echo reception process involves a subset of the transducer array, denoted by $\mathcal{M} \subseteq \{(m,n) | 1 \le m \le M, 1 \le n \le N\}$

$$\Phi(t; \theta_x, \theta_y) = \frac{1}{N_{\text{RX}}} \sum_{(m,n) \in \mathcal{M}} \hat{\varphi}_{m,n}(t; \theta_x, \theta_y). \qquad (6)$$

Here, $N_{\text{RX}} = |\mathcal{M}|$ is the number of transducers participating in the reception process. We note that in order to obtain optimal performance in terms of SNR and angular resolution, all transducer elements should be used. However, as mentioned in the introduction, the number of active elements is often reduced due to practical constraints.

In practice, beamforming is carried out digitally, rather than by manipulation of the analog signals. The signals detected at each element must be sampled at a sufficiently high rate to apply the high-resolution time shifts defined in (5). This implies that the signal is sampled at rates significantly higher than its Nyquist rate, to improve the system's beamforming resolution and to avoid artifacts caused by digital implementation of beamforming in time. From now on, we will denote this rate as the beamforming rate f_s, which usually varies from 4 to 10 times the transducer central frequency [1], [32].

We conclude this section by evaluating the number of samples typically required to obtain a single volume for some predefined image depth. Our evaluation is based on the imaging setup used in the simulation in Section V-A. The simulation assumes an ultrasonic scanner comprising a 32×32 grid of transducers, all of which are active both on transmission and reception ($N_{\text{RX}} = 1024$). Such an array constitutes a reference for comparison of image quality resulting from different methods for data rate reduction. The radial depth of the scan is set as $r = 5.5\,\text{cm}$ with a speed of sound of $c = 1540\,\text{m/s}$, yielding a time of flight of $T = 2r/c \simeq 71.43\,\mu\text{s}$. The acquired signal is characterized by a band-pass bandwidth of 1.4 MHz centered at a carrier frequency of $f_0 = 3\,\text{MHz}$. It is sampled at a rate of $f_s = 18.25\,\text{MHz}$ to provide sufficient beamforming resolution leading to $N = 1304$ samples taken at each transducer. Every frame contains 21×21 scan lines, such that the scanned volume is a square pyramid with an opening angle of $14.3°$. This set of scanning angles is a relatively narrow set with a typical margin between subsequent beam lines. Assuming all 1024 elements are sampled, the total number of samples that must be processed to display a single frame is $21 \times 21 \times 1024 \times 1304 = 5.89 \times 10^8$. This number of samples is huge even for a moderate imaging depth of 5.5 cm; the imaging depth typically required for cardiac imaging is around 16 cm. Achieving a reasonable frame rate using such an amount of samples is infeasible for any low-cost ultrasound machine. A common solution is to use a sparsely populated array of transducer elements. This typically causes reduction in angular resolution and, more significantly, low SNR. A method that reduces the amount of samples while using the entire transducer grid in the reception stage will address this problem.

III. Beamforming in Frequency

To substantially reduce the number of samples taken at each transducer element, we aim to use the low-rate sampling scheme proposed in [32]. To this end, we derive a frequency-domain formulation of 3-D beamforming allowing to compute the Fourier coefficients of the beam from the detected signals' low-rate samples. In this section, we show that similarly to 2-D imaging, the Fourier coefficients of the 3-D beam can be computed as a linear combination of the Fourier coefficients of the received signals. We note that due to the dynamic nature of beamforming, such a relationship is not trivial and requires appropriate justification.

A. Frequency-Domain Implementation of Beamforming

We start from the computation of the Fourier series coefficients of the beamformed signal $\Phi(t; \theta_x, \theta_y)$. It is shown in Appendix A that the support of $\Phi(t; \theta_x, \theta_y)$ is limited to $[0, T_B(\theta_x, \theta_y))$, where $T_B(\theta_x, \theta_y)$ is given by

$$T_B(\theta_x, \theta_y) = \min_{(m,n) \in \mathcal{M}} \tau_{m,n}^{-1}(T; \theta_x, \theta_y) \qquad (7)$$

with $\tau_{m,n}(t; \theta_x, \theta_y)$ defined in (5). Furthermore, $T_B(\theta_x, \theta_y) \le T$, where T is defined by the transmitted pulse penetration depth.

Consider the Fourier series of the beamformed signal $\{c[k]\}$ in the interval $[0, T]$

$$c[k] = \frac{1}{T} \int_0^T \Phi(t; \theta_x, \theta_y) I_{[0, T_B(\theta_x, \theta_y))} e^{-i\frac{2\pi}{T}kt} dt \qquad (8)$$

where $I_{[a,b]}$ is the indicator function, used to reduce noise since the useful information in $\Phi(t; \theta_x, \theta_y)$ is restricted to $[0, T_B(\theta_x, \theta_y))$. In order to find a relation between $c[k]$ and the Fourier coefficients of $\varphi_{m,n}(t; \theta_x, \theta_y)$, we substitute (6) into (8)

$$c[k] =$$
$$\frac{1}{N_{\text{RX}}} \sum_{(m,n) \in \mathcal{M}} \frac{1}{T} \int_0^T \hat{\varphi}_{m,n}(t; \theta_x, \theta_y) I_{[0, T_B(\theta_x, \theta_y))} e^{-i\frac{2\pi}{T}kt} dt$$
$$= \frac{1}{N_{\text{RX}}} \sum_{(m,n) \in \mathcal{M}} \hat{c}_{m,n}[k] \qquad (9)$$

where we defined

$$\hat{c}_{m,n}[k] = \frac{1}{T} \int_0^T \varphi_{m,n}(\tau_{m,n}(u; \theta_x, \theta_y); \theta_x, \theta_y)$$
$$\times I_{[0, T_B(\theta_x, \theta_y))} e^{-i\frac{2\pi}{T}ku} du. \qquad (10)$$

Replacing the integration variable u with $\tau = \tau_{m,n}(u; \theta_x, \theta_y)$, we get

$$u = \frac{\tau^2 - |\gamma_{m,n}|^2}{\tau - (\gamma_m x_\theta + \gamma_n y_\theta + \gamma_{m,n}^z z_\theta)}$$

$$du = \frac{\tau^2 + |\gamma_{m,n}|^2 - 2\tau \cdot (\gamma_m x_\theta + \gamma_n y_\theta + \gamma_{m,n}^z z_\theta)}{[\tau - (\gamma_m x_\theta + \gamma_n y_\theta + \gamma_{m,n}^z z_\theta)]^2} d\tau$$

where $x_\theta, y_\theta, z_\theta$ are defined in (2). Plugging this into (10) and renaming the integration variable $\tau \to t$, results in

$$\hat{c}_{m,n}[k] = \frac{1}{T} \int_0^T q_{k,m,n}(t; \theta_x, \theta_y) \varphi_{m,n}(t; \theta_x, \theta_y) e^{-i\frac{2\pi}{T}kt} dt \tag{11}$$

with

$$q_{k,m,n}(t; \theta_x, \theta_y) = I_{[|\gamma_{m,n}|, \tau_{m,n}(T_B(\theta_x, \theta_y); \theta_x, \theta_y))}(t)$$
$$\times \frac{t^2 + |\gamma_{m,n}|^2 - 2t \cdot (\gamma_m x_\theta + \gamma_n y_\theta + \gamma_{m,n}^z z_\theta)}{(t - (\gamma_m x_\theta + \gamma_n y_\theta + \gamma_{m,n}^z z_\theta))^2}$$
$$\times \exp\left\{-i\frac{2\pi}{T}k\left(\frac{t \cdot (\gamma_m x_\theta + \gamma_n y_\theta + \gamma_{m,n}^z z_\theta) - |\gamma_{m,n}|^2}{t - (\gamma_m x_\theta + \gamma_n y_\theta + \gamma_{m,n}^z z_\theta)}\right)\right\}. \tag{12}$$

Note that in contrast to (10), (11) contains a nondelayed version of $\varphi_{m,n}(t; \theta_x, \theta_y)$, while the delays are applied through the distortion function $q_{k,m,n}(t; \theta_x, \theta_y)$, defined in (12). This allows us to express $\varphi_{m,n}(t; \theta_x, \theta_y)$ in terms of its Fourier series coefficients, denoted by $c_{m,n}[l]$. We also make use of the Fourier coefficients of $q_{k,m,n}(t; \theta_x, \theta_y)$ with respect to $[0, T]$, denoted by $Q_{k,m,n;\theta_x,\theta_y}[l]$, and rewrite (11) as follows:

$$\hat{c}_{m,n}[k] = \sum_l c_{m,n}[l] \frac{1}{T} \int_0^T q_{k,m,n}(t; \theta_x, \theta_y) e^{-i\frac{2\pi}{T}(k-l)t} dt$$
$$= \sum_l c_{m,n}[k-l] Q_{k,m,n;\theta_x,\theta_y}[l]. \tag{13}$$

The substitution of the distortion function by its Fourier coefficients effectively transfers the beamforming delays defined in (5) to the frequency domain. We note that $q_{k,m,n}(t; \theta_x, \theta_y)$ is independent of the received signals, namely, it is defined solely by the array geometry. Its Fourier coefficients, therefore, are computed offline and stored as a look-up table (LUT).

According to Proposition 1 in [31], which can be easily extended to the 3-D imaging setup, $\hat{c}_{m,n}[k]$ may be approximated sufficiently well when we replace the infinite summation in (13) by a finite one

$$\hat{c}_{m,n}[k] \simeq \sum_{l=-L_1}^{L_2} c_{m,n}[k-l] Q_{k,m,n;\theta_x,\theta_y}[l]. \tag{14}$$

The Fourier coefficients of the beam $c[k]$ are now easily calculated by plugging (14) into (9)

$$c[k] \simeq \frac{1}{N_{RX}} \sum_{(m,n)\in\mathcal{M}} \sum_{l=-L_1}^{L_2} c_{m,n}[k-l] Q_{k,m,n;\theta_x,\theta_y}[l]. \tag{15}$$

The approximation in (14) relies on the decay properties of $\{Q_{k,m,n;\theta_x,\theta_y}[l]\}$. According to the results reported in [32], most of the energy of the Fourier coefficients of the 2-D distortion function is concentrated around the dc component, allowing for efficient implementation of beamforming in frequency. This decaying property is retained in 3-D beamforming: numerical studies show that most of the energy of $\{Q_{k,m,n;\theta_x,\theta_y}[l]\}$ is concentrated around the dc component, irrespective of the
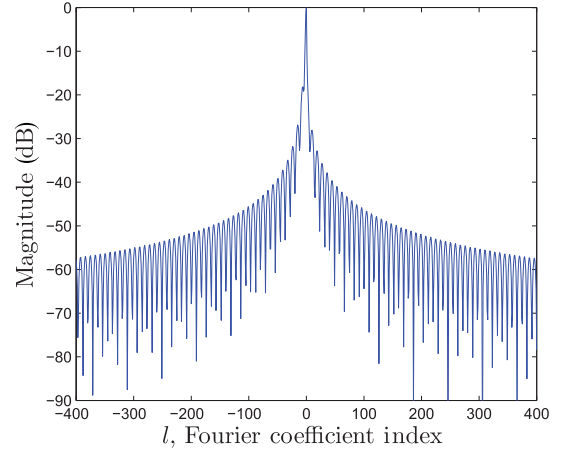

Fig. 2. $\{Q_{k,m,n;\theta_x,\theta_y}[l]\}$, the Fourier coefficients of $q_{k,m,n}(t; \theta_x, \theta_y)$, display a rapid decay around the dc component.

choice of $k, m, n, \theta_x, \theta_y$. We assume that for $l < -L_1$ and $l > L_2, \{Q_{k,m,n;\theta_x,\theta_y}[l]\}$ are several orders of magnitude lower and thus can be neglected. The choice of L_1, L_2 controls the approximation quality. We display these decay properties in Fig. 2, where $Q_{k,m,n;\theta_x,\theta_y}[l]$ is plotted as a function of l for $k = 300, m = 7, n = 21, \theta_x = 0.28(\text{rad})$, and $\theta_y = 0.36(\text{rad})$.

B. Rate Reduction by Beamforming in Frequency

We now show that FDBF allows generating a frame using a reduced number of samples of the individual signals in comparison time-domain beamforming. When the signal's structure is not considered, this is done by avoiding the oversampling factor required by digital implementation of time-domain beamforming. In this case, the processing is performed at the effective Nyquist rate defined by the signal's effective bandwidth. Further rate reduction can be obtained when the FRI structure of the beamformed signal is taken into account, and CS techniques are used for its recovery.

Using Xampling, we can obtain an arbitrary and possibly nonconsecutive set κ, composed of K frequency components of the individual detected signals, from K pointwise samples of the signal filtered with an analog kernel $s^*(t)$, designed according to κ. In ultrasound imaging with modulated Gaussian pulses, the transmitted signal has one main band of energy. As a result, the analog filter takes on the form of a band-pass filter, leading to a simple low-rate sampling scheme [32]. The choice of κ dictates the bandwidth of the filter and the resulting sampling rate.

As can be seen in (15), in order to calculate an arbitrary set κ of size $\mathcal{K}$ of Fourier coefficients of the beamformed signal, only $\mathcal{K} + L_1 + L_2$ Fourier coefficients of each one of the individual signals are required. The image line is then reconstructed from the beamformed signal's Fourier coefficients $\{c[k]\}$. Calculating the entire set of Fourier coefficients in the bandwidth of the beamformed signal $\beta, |\beta| = B$, implies $B \gg L_1 + L_2$ and, therefore, allows one to obtain all the information in the frequency domain while avoiding oversampling required by time-domain beamforming. This is due to the fact that the low-rate sampling scheme described above obtains

$B + L_1 + L_2 \approx B$ Fourier coefficients of the individual signals required for FDBF from their B low-rate samples.

Thus, performing FDBF by calculating the entire bandwidth of the beamformed signal achieves a rate reduction of approximately N/B with respect to time-domain beamforming, where N is the number of samples required by the beamforming rate f_s.

Further rate reduction is possible by acquiring a part of the bandwidth of the beamformed signal, $\mu \subset \beta$, $|\mu| = M$. We may calculate it from $M + L_1 + L_2 \approx M$ samples of the individual signals, which are sampled at a rate that is N/M lower than the standard beamforming rate f_s. In Section IV, we take advantage of the beamformed signal structure to reconstruct the beam from its partial frequency data. A detailed discussion on the achieved rate reduction is provided in Section V-A.

IV. RECOVERY FROM SUB-NYQUIST SAMPLES

When all the beam's Fourier coefficients within its effective bandwidth are computed, the beam in time is recovered by an inverse Fourier transform. When only a subset of the coefficients is obtained by sub-Nyquist sampling and processing, we exploit the structure of the beam to reconstruct it from its partial frequency data.

According to [24], we may model the detected signals at the individual transducer elements, $\{\varphi_{m,n}(t;\theta_x,\theta_y)\}_{(m,n)\in\mathcal{M}}$, as FRI signals. That is, we assume that the individual signals can be regarded as a sum of pulses, all replicas of a known transmitted pulse shape

$$\varphi_{m,n}(t;\theta_x,\theta_y) = \sum_{l=1}^{L} \tilde{a}_{l,m,n} h(t - t_{l,m,n}). \qquad (16)$$

Here, $h(t)$ is the transmitted pulse shape, L is the number of scattering elements in the direction of the transmitted pulse (θ_x, θ_y), $\{\tilde{a}_{l,m,n}\}_{l=1}^{L}$ are the unknown amplitudes of the reflections, and $\{t_{l,m,n}\}_{l=1}^{L}$ are the times at which the reflection from the lth scatterer arrives at the (m, n) element.

It is shown in Appendix B that the beamformed signal in 3-D imaging approximately satisfies the FRI model, just as it does in 2-D imaging [31]. Namely, it can be written as

$$\Phi(t;\theta_x,\theta_y) \simeq \sum_{l=1}^{L} \tilde{b}_l h(t - t_l) \qquad (17)$$

where $h(t)$ and L are defined as above, $\{\tilde{b}_l\}_{l=1}^{L}$ are the unknown amplitudes of the reflections, and $\{t_l\}_{l=1}^{L}$ are the times at which the reflection from the lth scatterer arrives at the reference element (m_0, n_0).

Having acquired the Fourier coefficients $c[k]$ as described in the previous section, we now wish to reconstruct the beamformed signal. Since the beam satisfies the FRI model, our task is to extract the unknown parameters, $\{\tilde{b}_l\}_{l=1}^{L}$ and $\{t_l\}_{l=1}^{L}$, that describe it.

Using (17), the Fourier coefficients of $\Phi(t;\theta_x,\theta_y)$ are given by

$$c[k] = \frac{1}{T} \int_0^T \Phi(t;\theta_x,\theta_y)e^{-i\frac{2\pi}{T}kt}$$

$$\simeq \frac{1}{T} \int_0^T \left(\sum_{l=1}^{L} \tilde{b}_l h(t - t_l) \right) e^{-i\frac{2\pi}{T}kt}$$

$$= \sum_{l=1}^{L} \tilde{b}_l \left(\frac{1}{T} \int_0^T h(t - t_l)e^{-i\frac{2\pi}{T}k(t-t_l)} \right) e^{-i\frac{2\pi}{T}kt_l}$$

$$= h[k] \sum_{l=1}^{L} \tilde{b}_l e^{-i\frac{2\pi}{T}kt_l} \qquad (18)$$

where $h[k]$ is the kth Fourier coefficient of $h(t)$. By quantizing the delays $\{t_l\}_{l=1}^{L}$ with quantization step $T_s = \frac{1}{f_s}$, such that $t_l = q_l T_s$ for $q_l \in \mathbb{Z}$, we may write the Fourier coefficients of the beamformed signal as

$$c[k] = h[k] \sum_{l=0}^{N-1} b_l e^{-i\frac{2\pi}{N}kl}. \qquad (19)$$

Here, $N = \lfloor T/T_s \rfloor$, $b_l = \tilde{b}_l \delta_{l,q_l}$, and $\delta_{a,b}$ is the Kronecker delta.

We conclude that recovering the beamformed signal in time is equivalent to determining b_l in (19) for $0 \le l \le N - 1$. In vector–matrix notation, (19) can be rewritten as

$$c = \mathbf{H}\mathbf{D}b = \mathbf{A}b \qquad (20)$$

where c is a vector of length $\mathcal{K}$ with kth entry $c[k]$, $\mathbf{H}$ is a $\mathcal{K} \times \mathcal{K}$ diagonal matrix with kth entry $h[k]$, $\mathbf{D}$ is a $\mathcal{K} \times N$ matrix whose rows are taken from the $N \times N$ discrete fourier transform (DFT) matrix corresponding to the relevant Fourier indices of $\Phi(t;\theta_x,\theta_y)$, and b is a column vector of length N with lth entry b_l.

We wish to extract the values of b, which fully describe the beamformed signal. To do so, we rely on the assumption that a typical ultrasound image is composed of a relatively small number of strong reflectors in the scanned tissue. In other words, we assume the vector b to be compressible, similarly to [32]. We then find b by solving an ℓ_1 optimization problem

$$\min_{b} \|b\|_1 \text{ s.t. } \|\mathbf{A}b - c\|_2 \le \varepsilon. \qquad (21)$$

In practice, we solve (21) using the NESTA algorithm [37] which works well when the signal of interest has high dynamic range. NESTA uses a single smoothing parameter μ selected based on a tradeoff between accuracy and speed of convergence. We choose this parameter empirically to achieve optimal performance with respect to image quality.

To summarize this section, a step-by-step description of the 3-D low-rate imaging process is given in Algorithm 1.

V. SIMULATIONS AND RESULTS

To analyze the performance of the outlined methodology relative to standard time-domain beamforming in a manner independent of the specifics of any individual system, a *k-Wave* [38] simulation of a 3-D ultrasound system is presented. We first simulate the acoustic imaging of a noise free volume

Algorithm 1. Image acquisition algorithm

1: Calculate the Fourier coefficients of $q_{j,m,n}(t; \theta_x, \theta_y)$, defined in (12). This calculation is performed offline and does not affect the system's real-time performance.
2: Choose the approximation quality by determining L_1, L_2, defined according to the decay properties of $\{Q_{k,m,n;\theta_x,\theta_y}[l]\}_l$, displayed in Fig. 2. An adequate approximation can be performed by choosing L_1, L_2 to be no greater than 10.
3: Choose a subset κ of Fourier coefficients of the beamformed signal to be used in reconstruction.
4: Acquire the Fourier coefficients of the individual signals relevant for reconstruction of the subset κ, according to [32]. Namely, at each transducer element $(m, n) \in \mathcal{M}$, acquire its Fourier coefficients $\{c_{m,n}[l]\}_{l=k_1+L_1}^{k_2+L_2}$, where k_1, k_2 are the lowest and highest indices in κ.
5: Perform the calculation in (14).
6: Compute the beamformed signal's Fourier series coefficients:

$$c[k] = \frac{1}{N_{\mathrm{RX}}} \sum_{(m,n)\in\mathcal{M}} \hat{c}_{m,n}[k].$$

7: Solve the optimization problem (21) to extract the vector $\mathbf{b}$ that characterizes the beamformed signal.
8: Incorporate the known temporal shape of the pulses, $h(t)$, onto the vector $\mathbf{b}$, and perform standard postprocessing steps, such as log-compression and interpolation.

---

containing three point scatterers and analyze the effect of the achieved rate reduction on the lateral and APSFs. The performance of low-rate 3-D FDBF is compared to that of standard time-domain processing.

An alternative approach to reduce the number of samples is to use a sparse array upon reception, which also reduces the hardware complexity. To evaluate the effect of element number reduction on image quality, time-domain beamforming is also performed using data collected only from the elements placed along the array's main diagonals. The results verify that the two strategies affect different aspects of image quality and show the advantage of 3-D FDBF in the presence of noise compared to time-domain beamforming with the reduced number of elements. Finally, we incorporate the proposed approach into a commercial imaging system performing subarray beamforming to reduce the number of receiving elements. In this setup, the element reduction and 3-D FDBF are applied in conjunction. The results show that rate reduction obtained by 3-D FDBF does not introduce further image quality degradation.

A. Simulation Setup

We simulate acoustic imaging of a volume of size 28 mm × 28 mm × 55 mm. The volume contains three point reflectors, placed at depths 26, 31.5, and 37 mm from the center of a square planar 2-D transducer grid. The reflectors are located around $\theta_x = -7.5°$, $0°$, and $7.5°$, respectively, with $\theta_y = 0°$. The reflector at depth 31.5 mm is located at the focus point of the

TABLE I
NUMBER OF SAMPLES PER VOLUME FOR EACH PROCESSING METHOD

Processing method	Number of samples
Time Full grid	5.89×10^8
Time Diagonal grid	36.81×10^6
Frequency B coefficients	99.8×10^6
Frequency $B/2$ coefficients	54.64×10^6
Frequency $B/3$ coefficients	39.74×10^6

transmitted pulse. The array is composed of $32 \times 32 = 1024$ elements, spaced 140 μm apart. The central pulse frequency is 3 MHz with a bandwidth of 1.4 MHz and the sampling rate is $f_s = 18.25$ MHz. A penetration depth of $T = 2r/c \simeq 71.43$ μs yields $N = 1304$ samples at each transducer element, so that the bandwidth of the beamformed signal contains $B = 200$ Fourier coefficients. A single volume comprises 21×21 scanned angles.

Denote by κ the set of Fourier coefficients of the beam, obtained by the proposed method. To verify the performance for different rate reduction factors, the collected data are processed using our technique with $\mathcal{K} = B$, $\mathcal{K} = B/2$, and $\mathcal{K} = B/3$ corresponding to the entire, half, and one third of the effective bandwidth, respectively, where $\mathcal{K}$ is the cardinality of κ. The results are compared to those obtained by time-domain beamforming performed both using full and diagonal grids upon reception.

First, we assess the amount of samples required to obtain a volume. For time-domain beamforming using the full grid, we must process $21 \times 21 \times 1024 \times N = 5.89 \times 10^9$ samples. Using only the main diagonals of the transducer grid, this amount reduces to $21 \times 21 \times 64 \times N = 36.81 \times 10^6$ samples. Applying FDBF, the reconstruction relied on $\mathcal{K} = 200$, $\mathcal{K} = 100$, and $\mathcal{K} = 67$ Fourier coefficients of the beamformed signal. To calculate these coefficients, as described in Section III, we chose $L_1 = L_2 = 10$. The total amount of Fourier coefficients required at each transducer is $\nu = \mathcal{K} + L_1 + L_2$. A sampling approach proposed in [32] allows us to obtain these coefficients from ν samples of individual detected signals. Thus, a single volume can be produced by processing a total of $21 \times 21 \times 1024 \times \nu$ samples. The total number of samples required for each processing method is displayed in Table I. We note that FDBF, using about half the bandwidth of the beam, is comparable to time-domain processing using only the diagonal elements of the grid in terms of processing rate.

Cross sections of the resulting 3-D volumes are displayed in Fig. 3. It can be seen that all reflectors are clearly seen for all processing methods. The frequency-domain beamformed images display lower noise levels than the time-domain beamformed image reconstructed using a partial set of the transducer grid. The advantage of FDBF in the presence of noise is discussed in detail in Section V-C.

B. Lateral and APSFs

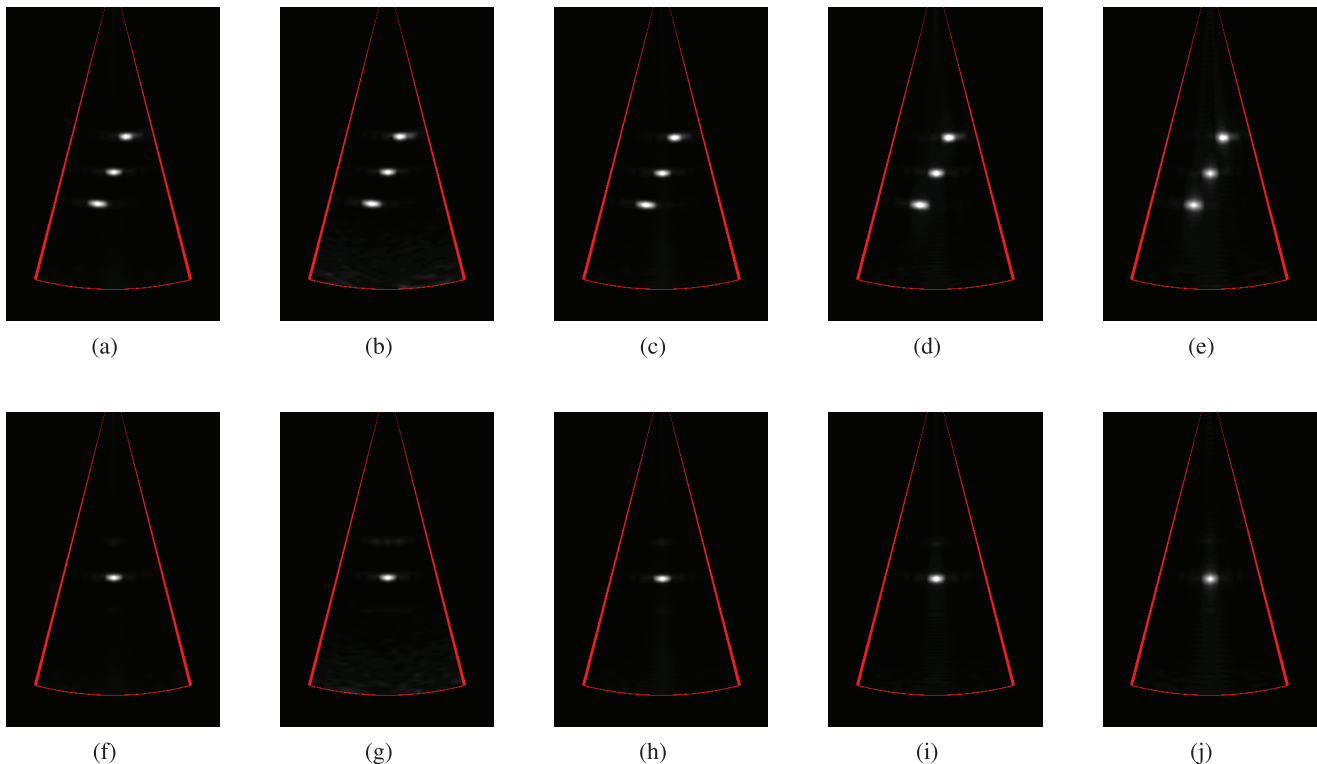We next compare our proposed method to time-domain beamforming by calculating the LPSF and APSF characterizing

Fig. 3. Cross sections of the simulated 3-D imaging of three point reflectors placed on a plane. (a)–(e) display the $\theta_y = 0°$ cross section, whereas (f)–(j) display the $\theta_x = 0°$ cross section. (a) and (f) display images acquired with time-domain beamforming, using the entire transducer grid. (b) and (g) display images acquired with time-domain beamforming, using the diagonals of the transducer grid. (c) and (h), (d) and (i), (e) and (j) display images acquired with FDBF using B, $B/2$, and $B/3$ DFT coefficients of the beamformed signal, respectively.
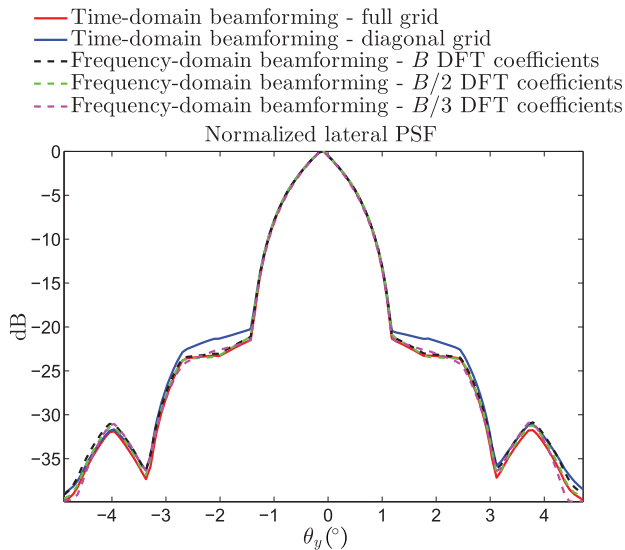

Fig. 4. Normalized LPSFs for various processing methods.

each processing method. The LPSFs are acquired for the reflector placed at the transmit focus point and plotted on constant-r arcs. The APSFs show the sum of the constant—θ_x and θ_y lines on which point reflectors are placed. The LPSFs are normalized such that the maximum at $\theta_y = 0°$ is set to 1, while the APSFs are normalized to unit energy. The PSFs are presented in Figs. 4 and 5.

The properties of the LPSFs are displayed in Table II. We see that the LPSFs obtained with 3-D FDBF for different rate

reduction factors display very similar properties to the LPSF acquired with time-domain beamforming using the full transducer grid and exhibit improved results over the LPSF acquired with time-domain beamforming using only the diagonals of the grid. This is an expected result, since our method reconstructs the axial lines of the image and does not have a direct effect on the lateral resolution. The widths of the peak located at the focus point, acquired for each reconstructed method, are shown in Table III. As seen in the table and in Fig. 5, the APSFs deteriorate when the number of Fourier coefficients used to reconstruct the image is decreased. We note that energy leakage from the peaks is increased when less Fourier coefficients are used in the reconstruction process. However, the effect of APSF deterioration becomes visible only when less than half the bandwidth is used for signal reconstruction.

Reducing the amount of transducer elements enhances noise levels in the image and deteriorates the lateral resolution, while our proposed reconstruction method affects mainly the axial resolution. Acknowledging this fact, we may consider a midway approach, where rate reduction is achieved both by reducing the amount of transducer elements and applying frequency-domain beamforming. The more dominant factor for rate reduction will be dictated according to the tradeoff stated above. Another conclusion is that when the element number reduction is unavoidable, the incorporation of 3-D FDBF does not cause further degradation in lateral resolution and SNR, while providing additional data rate reduction.

In addition to the axial and lateral resolutions, another important aspect that has to be regarded is the SNR. It can be seen

TABLE II
LPSFs PROPERTIES

Processing method	Full width at half maximum (°)	Average sidelobes (dB)	First sidelobe's peak (dB)
Time Full grid	1.50	−29.63	−22.93
Time Diagonal grid	1.51	−28.53	−21.40
Frequency B coefficients	1.51	−29.01	−22.70
Frequency $B/2$ coefficients	1.52	−29.37	−22.90
Frequency $B/3$ coefficients	1.47	−29.47	−22.74

TABLE III
APSFs PROPERTIES

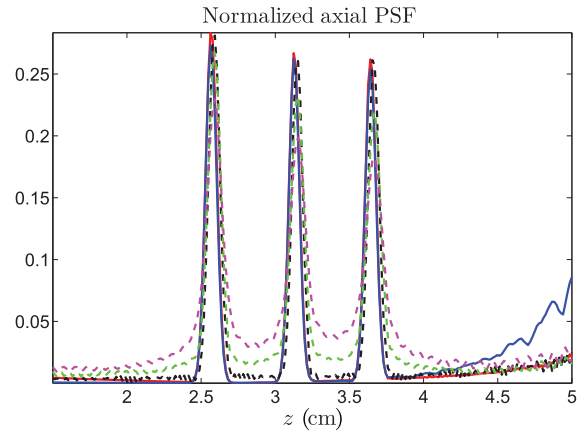| Processing method	Full width at half maximum (mm)
Time Full grid	0.084
Time Diagonal grid	0.082
Frequency B coefficients	0.086
Frequency $B/2$ coefficients	0.107
Frequency $B/3$ coefficients	0.138

Fig. 5. Normalized APSFs for various processing methods.

TABLE IV
SNR OF PROCESSING METHODS

Processing method	SNR (dB)
Time Full grid	20.83
Time Diagonal grid	8.92
Frequency B coefficients	26.69
Frequency $B/2$ coefficients	28.68
Frequency $B/3$ coefficients	29.48

in Fig. 5 that the line acquired with time-domain beamforming using partial grid data contains high levels of noise at the far field, since less transducer elements participate in the delay-and-sum process. This holds even when no noise was incorporated in the simulation—the "effective noise" stems from reflections corresponding to the numerical solution of the simulation code.

C. Simulation With Noise

To show the advantage of our method over partial grid time-domain beamforming in terms of SNR, another simulation is conducted. A pulse is transmitted in the $\theta_x = 0, \theta_y = 0$ direction. A single large reflector is placed at the focus depth of the transmitted pulse. The signals detected at the transducer elements are contaminated by white Gaussian noise imitating the thermal noise of the system. We then proceed to reconstruct the $\theta_x = 0, \theta_y = 0$ beam using all five methods described in Section V-A. In addition, clean beams, without the addition of noise, are obtained for all five methods. We denote the noisy and clean beamformed lines by $\Phi_{\text{noise}}(t)$ and $\Phi_{\text{clean}}(t)$, respectively.

We define the SNR of a beam as the ratio between the energy stored in a segment of length 5λ around the main peak of the beam, where λ is the wavelength corresponding to the carrier frequency of the transmitted pulse, and the energy of the noise in the beamformed line, defined as $n(t) = \Phi_{\text{noise}}(t) - \Phi_{\text{clean}}(t)$. That is,

$$\text{SNR} = 10 \log_{10} \left(\frac{\int |\Phi_{\text{clean}}(t)|^2 dt}{\int |n(t)|^2 dt} \right). \tag{22}$$

The results are displayed in Table IV. As expected, the reduction in number of elements participating leads to a dramatic

reduction in SNR. In contrast, 3-D FDBF displays higher SNR even over time-domain processing when the entire grid of transducer elements is used. A remarkable point is that the SNR increases when less Fourier coefficients are involved in the reconstruction of the beam. This is not surprising since the noise is equally spaced over the entire spectrum of the system: the fewer Fourier coefficients used in the reconstruction process, the less noise involved.

To conclude, 3-D FDBF using half the bandwidth is comparable to standard time-domain processing with diagonal transducer elements in terms of data rate reduction but outperforms it by 20 dB in terms of SNR.

D. Application on a Commercial System

We now demonstrate our method on data collected using a commercial 3-D ultrasound system, while imaging a phantom of a heart ventricle. Images of the entire volumetric scan, taken from a specific angle, for demonstration are shown in Fig. 6. The frames are reconstructed using time-domain beamforming and frequency-domain beamforming with $\mathcal{K} = B/2$ coefficients of the beamformed signal. The complex structure of the phantom allows us to test the performance of the proposed method on volumes containing multiple strong reflectors as well as weak reflectors known as speckle.
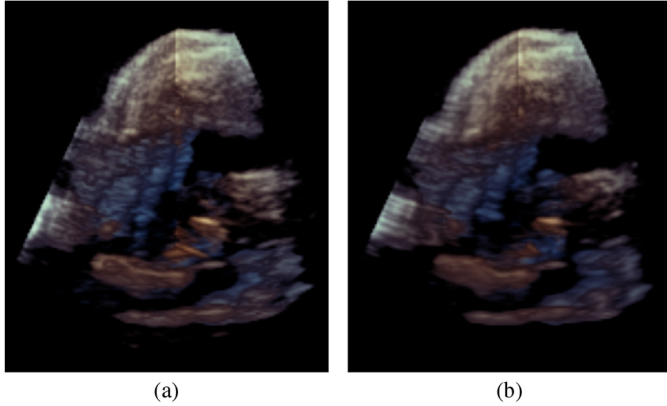
(a)   (b)

Fig. 6. 3-D imaging of a phantom of a heart ventricle. (a) displays the time-domain reconstruction of the frame, while (b) displays the frequency-domain reconstructed frame, using $\mathcal{K} = B/2$ Fourier coefficients of the beamformed signal with 12-fold rate reduction.

The transducer grid is composed of 2000 transducers. The entire grid participates in the transmission stage, while analog subarray beamforming [15] is performed in the reception stage. This suboptimal processing method is required to adjust the number of elements to the number of electronic channels. To put it explicitly, an appropriate constant analog delay is applied on a group of 20 elements prior to summation. The resulting 100 signals are treated as effective elements. In standard processing, they are sampled and fed to electronic channels for dynamic beamforming. To verify the performance of the proposed method, FDBF is applied on the resulting 100 signals instead of time-domain processing following the analog subarray beamforming stage.

We processed the collected data in the same manner as in the previous section, using time-domain beamforming requiring 3120 samples per image line, and FDBF for $\mathcal{K} = B$ and $\mathcal{K} = B/2$ with $B = 506$. When B Fourier coefficients are computed, the processing is performed at the signal's effective Nyquist rate and oversampling is avoided leading to 6-fold rate reduction. FDBF with $B/2$ coefficients implies 12-fold rate reduction. Cross sections of the 3-D frames acquired are displayed in Fig. 7.

The image obtained by low-rate FDBF for $\mathcal{K} = B$ is virtually identical to the one obtained by standard time-domain processing at a high rate. This result is expected since for $\mathcal{K} = B$ all the information is obtained in frequency. We also note prominent similarity between the image obtained at the sub-Nyquist rate and the original one. In particular, the strong reflectors and the speckle pattern are preserved. The above results prove that FDBF can be combined with analog subarray beamforming without significant reduction in image quality. In this way, channel number reduction resulting from analog subarray processing is combined with sampling rate reduction obtained by FDBF paving the way to real-time low-cost 3-D imaging system.

VI. Conclusion

In this work, a solution to one of the major bottlenecks in 3-D imaging, the amount of sampled data, is introduced. The number of samples taken at each transducer element is reduced by applying the low-rate sampling scheme presented in [32] to the individual signals detected by the 2-D grid. To benefit from the achieved data rate reduction, we prove that the subsequent processing, namely, 3-D beamforming, can be performed directly in frequency. The translation of beamforming to the frequency domain allows bypassing oversampling and to obtain 4- to 10-fold rate reduction without any assumptions on the signal's structure.

When the signal's structure is exploited further rate reduction is possible. We prove that the 3-D beamformed signal obeys an FRI model, allowing to sample and process the signals at sub-Nyquist rates while retaining sufficient image quality.

The performance of the proposed method is verified in terms of both LPSF and APSF. It is shown that in accordance with our expectation, it has no effect on LPSF, while the APSF is virtually the same when the entire set of Fourier coefficients of the beam within its effective bandwidth is computed. For sub-Nyquist processing APSF is slightly reduced; however, when half the beam's bandwidth is used, the degradation is negligible. We also demonstrate the advantage of 3-D FDBF in the presence of noise. The simulations with noise show that low-rate 3-D FDBF outperforms not only time-domain processing with a partial grid of elements, but also the time-domain processing with a full grid.

Finally, we incorporate the proposed framework into a commercial imaging system and combine it with analog subarray beamforming, required to adjust the number of elements to the number of electronic channels. The results verify that no further image degradation is introduced and that our approach can be used in conjunction with spatial subsampling techniques.

Our results pave the way for low-cost real-time capability crucial for further development of 3-D ultrasound imaging.

Appendix A
Beamformed Signal Support

We consider the FRI model for the individual signals in (16). According to our second assumption in Appendix B, $h(t)$ is the known pulse-shape with a support of $[0, \Delta)$ for some known Δ satisfying $\Delta \ll T$.

We neglect all reflections that reach the (m, n) transducer at times greater than T, considering them as noise. Therefore, for all $1 \leq l \leq L$ and $(m, n) \in \mathcal{M}$

$$t_{l,m,n} + \Delta \leq T. \tag{23}$$

Using (31), (23) and the fact that $\tau_{m,n}(t; \theta_x, \theta_y)$ is nondecreasing for $t \geq 0$, we get

$$t_l \leq \tau_{m,n}^{-1}(T - \Delta; \theta_x, \theta_y) \tag{24}$$

with $\tau_{m,n}^{-1}(t; \theta_x, \theta_y)$ being the inverse of $\tau_{m,n}(t; \theta_x, \theta_y)$ with respect to t

$$\tau_{m,n}^{-1}(t; \theta_x, \theta_y) = \frac{t^2 - |\gamma_{m,n}|^2}{t - (\gamma_m x_\theta + \gamma_n y_\theta + \gamma_{m,n}^z z_\theta)} \tag{25}$$

for $t \geq |\gamma_{m,n}|$. Assuming the pulse shape has a negligible support with respect to the penetration depth, $\Delta \ll T$, and using
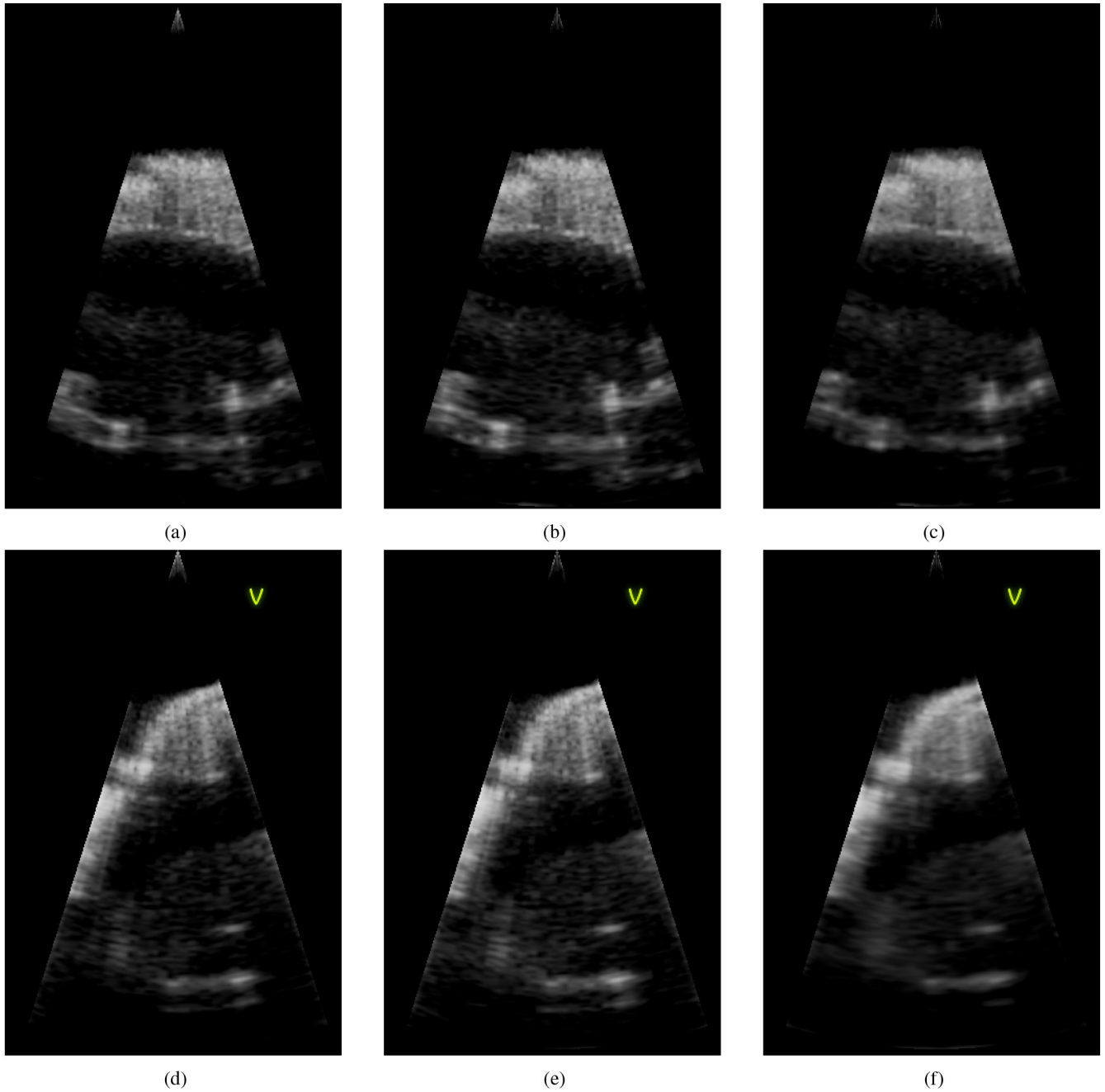
Fig. 7. Cross sections of the 3-D imaging of a phantom of a heart ventricle. (a)–(c) display the $\theta_y = 0°$ cross section, whereas (d)–(f) display the $\theta_x = 0°$ cross section. (a) and (d) display images acquired using time-domain beamforming. (b), (e) and (c), (f) display images acquired with frequency-domain beamforming with 6- and 12-fold rate reduction, respectively.

the fact that (24) holds for all $(m, n) \in \mathcal{M}$, we get, for all $1 \leq l \leq L$

$$t_l \leq \min_{(m,n)\in\mathcal{M}} \tau_{m,n}^{-1}(T; \theta_x, \theta_y). \tag{26}$$

Since $\{t_l\}_{l=1}^{L}$ denote the arrival times of the echoes to the reference element, we can set the upper bound $T_B(\theta_x, \theta_y)$ on the beamformed signal as

$$T_B(\theta_x, \theta_y) = \min_{(m,n)\in\mathcal{M}} \tau_{m,n}^{-1}(T; \theta_x, \theta_y). \tag{27}$$

We are now left to show that $T_B(\theta_x, \theta_y) < T$. This holds since we can always find an element $(m_1, n_1) \in \mathcal{M}$ such

that γ_{m_1} and γ_{n_1} have opposite signs to that of x_θ and y_θ, respectively. Furthermore, we can always place the reference element (m_0, n_0) such that $\gamma_{m_1,n_1}^z = 0$ for a specific choice of $(m_1, n_1) \in \mathcal{M}$. Thus,

$$
\begin{aligned}
T_B(\theta_x, \theta_y) &\leq \tau_{m_1,n_1}^{-1}(T; \theta_x, \theta_y) \\
&= \frac{T^2 - |\gamma_{m_1,n_1}|^2}{T + |\gamma_{m_1} x_\theta| + |\gamma_{n_1} y_\theta|} \\
&\leq \frac{T^2 - |\gamma_{m_1,n_1}|^2}{T} \\
&\leq T.
\end{aligned}
\tag{28}
$$

By applying $\tau_{m,n}(t; \theta_x, \theta_y)$ on both sides of (27), we also have

$$\tau_{m,n}(T_B(\theta_x, \theta_y); \theta_x, \theta_y) \leq T. \tag{29}$$

APPENDIX B
FRI MODEL OF THE BEAMFORMED SIGNAL

We assumed in (16) that the individual signals obey the FRI model. We wish to prove that the beamformed signal approximately obeys the FRI model, so that (17) holds.

In order to show this, we rely on three reasonable assumptions. First, we assume that $2(|\gamma_m| + |\gamma_n| + |\gamma_{m,n}^z|) \leq t_l$. Such a constraint may be forced by applying time-dependent apodization, in such a way that $\varphi(t; \theta_x, \theta_y)$ is omitted from the delay and sum process in (6) for $t \geq 2(|\gamma_m| + |\gamma_n| + |\gamma_{m,n}^z|)$. Second, we assume that the pulse $h(t)$, transmitted to the medium from each of the individual transducer elements and reflected back from scatterers in the medium, is compactly supported on the interval $[0, \Delta)$. Finally, we assume $\Delta \ll t_l$. Again, such a constraint may be forced by applying apodization.

Using (16), the individual distorted signals in (6) are of the form

$$\hat{\varphi}_{m,n}(t; \theta_x, \theta_y) = \sum_{l=1}^{L} \tilde{a}_{l,m,n} h(\tau_{m,n}(t; \theta_x, \theta_y) - t_{l,m,n}). \tag{30}$$

The resulting signal comprises L pulses, which are distorted versions of the pulse $h(t)$.

Suppose that some of these pulses originated in reflectors located off the central beam axis. When we combine the individual signals in (6) to calculate the beamformed signal, these pulses will be attenuated due to destructive interference. Therefore, when considering the beamformed signal $\Phi(t; \theta_x, \theta_y)$, we are concerned only with the pulses which originated in reflectors located along the central beam axis. For convenience, we assume that all pulses in (30) satisfy this property—those that do not will vanish in $\Phi(t; \theta_x, \theta_y)$.

The time of arrival at the (m, n) element $t_{l,m,n}$ is related to the time of arrival at the (m_0, n_0) element according to the alignment introduced in (5). Thus, we can express the delays of the individual signals, $\{t_{l,m,n}\}_{l=1}^{L}$, in terms of t_l, as

$$t_{l,m,n} = \tau_{m,n}(t_l; \theta_x, \theta_y). \tag{31}$$

We may then rewrite (30) as

$$\hat{\varphi}_{m,n}(t; \theta_x, \theta_y) = \sum_{l=1}^{L} \tilde{a}_{l,m,n} \tilde{h}(t; \theta_x, \theta_y) \tag{32}$$

where $\tilde{h}(t; \theta_x, \theta_y) = h(\tau_{m,n}(t; \theta_x, \theta_y) - \tau_{m,n}(t_l; \theta_x, \theta_y))$.

Applying our second assumption, we find that the support of $\tilde{h}(t; \theta_x, \theta_y)$ is defined by the requirement

$$0 \leq \tau_{m,n}(t; \theta_x, \theta_y) - \tau_{m,n}(t_l; \theta_x, \theta_y) < \Delta. \tag{33}$$

It can be shown that the inequalities in (33) are satisfied for $t \in [t_l, t_l + \Delta')$, where

$$\Delta' = 2\Delta \frac{t_{l,\theta} + \Delta}{t_{l,\theta} + 2\Delta + t_l - 2(\gamma_m x_\theta + \gamma_n y_\theta + \gamma_{m,n}^z z_\theta)} \tag{34}$$

and we defined

$$t_{j,\theta} = \sqrt{t_l^2 + 4|\gamma_{m,n}|^2 - 4t_l(\gamma_m x_\theta + \gamma_n y_\theta + \gamma_{m,n}^z z_\theta)}. \tag{35}$$

Since $2(|\gamma_m| + |\gamma_n| + |\gamma_{m,n}^z|) \leq t_l$ and the fact that $|x_\theta|, |y_\theta|, |z_\theta| \leq 1$, we have

$$t_l - 2(\gamma_m x_\theta + \gamma_n y_\theta + \gamma_{m,n}^z z_\theta)$$
$$\geq t_l - 2(|\gamma_m x_\theta| + |\gamma_n y_\theta| + |\gamma_{m,n}^z z_\theta|)$$
$$\geq t_l - 2(|\gamma_m| + |\gamma_n| + |\gamma_{m,n}^z|)$$
$$\geq 0.$$

Thus, $\Delta' \leq 2\Delta$, and therefore $\tilde{h}(t; \theta_x, \theta_y) = 0$ for $t \notin [t_l, t_l + 2\Delta)$. Let us write any $t \in [t_l, t_l + 2\Delta)$ as $t = t_l + \eta$, with $0 \leq \eta < 2\Delta$. Then,

$$\tilde{h}(t; \theta_x, \theta_y) = h(\tau_{m,n}(t_l + \eta; \theta_x, \theta_y) - \tau_{m,n}(t_l; \theta_x, \theta_y)). \tag{36}$$

Using our second assumption that $\Delta \ll t_l$ and $\eta < 2\Delta$, we have $\eta \ll t_l$. We then approximate the argument of $h(\cdot)$ in (36) to first order

$$\tau_{m,n}(t_l + \eta; \theta_x, \theta_y) - \tau_{m,n}(t_l; \theta_x, \theta_y). \tag{37}$$

To find the support explicitly, we expand the above inequality. For the left-hand side, we find that

$$\tau_{m,n}(t; \theta_x, \theta_y) - \tau_{m,n}(t_l; \theta_x, \theta_y) = \sigma_{l,m,n}(\theta_x, \theta_y) + o(\eta^2) \tag{38}$$

where

$$\sigma_{l,m,n}(\theta_x, \theta_y)$$
$$= \frac{1}{2} \left(1 + \frac{t_l - 2(\gamma_m x_\theta + \gamma_n y_\theta + \gamma_{m,n}^z z_\theta)}{\sqrt{t_l^2 - 4(\gamma_m x_\theta + \gamma_n y_\theta + \gamma_{m,n}^z z_\theta)t_l + 4|\gamma_{m,n}|^2}} \right). \tag{39}$$

We now extend our assumption that $2(|\gamma_m| + |\gamma_n| + |\gamma_{m,n}^z|) \leq t_l$, and assume that $|\gamma_m| + |\gamma_n| + |\gamma_{m,n}^z| \ll t_l$. Hence, $|\gamma_{m,n}| = \sqrt{|\gamma_m|^2 + |\gamma_n|^2 + |\gamma_{m,n}^z|^2} < |\gamma_m| + |\gamma_n| + |\gamma_{m,n}^z| \ll t_l$. Using this assumption, we get $\sigma_{l,m,n}(\theta_x, \theta_y) \to 1$. Replacing $\eta = t - t_l$ and substituting back to (36), results in

$$\tilde{h}(t; \theta_x, \theta_y) \approx h(t - t_l), t \in [t_l, t_l + 2\Delta).$$

Combining this result with (32) and using the fact that $h(t - t_l) = 0$ for $t \notin [t_l, t_l + 2\Delta)$, we get

$$\hat{\varphi}_{m,n}(t; \theta_x, \theta_y) \approx \sum_{l=1}^{L} \tilde{a}_{l,m,n} h(t - t_l). \tag{40}$$

Finally, plugging this back into (6)

$$\Phi(t; \theta_x, \theta_y) = \frac{1}{N_{\text{RX}}} \sum_{(m,n) \in \mathcal{M}} \hat{\varphi}_{m,n}(t; \theta_x, \theta_y)$$

$$\approx \frac{1}{N_{\text{RX}}} \sum_{(m,n) \in \mathcal{M}} \sum_{l=1}^{L} \tilde{a}_{l,m,n} h(t - t_l)$$

$$= \sum_{l=1}^{L} \frac{1}{N_{\text{RX}}} \sum_{(m,n) \in \mathcal{M}} \tilde{a}_{l,m,n} h(t - t_l)$$

$$= \sum_{l=1}^{L} \tilde{b}_l h(t - t_l) \qquad (41)$$

showing that the beamformed signal obeys an FRI model.

REFERENCES

[1] B. D. Steinberg, "Digital beamforming in ultrasound," *IEEE Trans. Ultrason., Ferroelectr., Freq. Control*, vol. 39, no. 6, pp. 716–721, Nov. 1992.

[2] R. W. Prager, U. Z. Ijaz, A. H. Gee, and G. M. Treece, "Three-dimensional ultrasound imaging," *Proc. Inst. Mech. Eng. H, J. Eng. Med.*, vol. 224, no. 2, pp. 193–223, 2010.

[3] K. Abo *et al.*, "Usefulness of transthoracic freehand three-dimensional echocardiography for the evaluation of mitral valve prolapse," *J. Cardiol.*, vol. 43, no. 1, pp. 17–22, 2004.

[4] J. Kwan, "Three-dimensional echocardiography: A new paradigm shift," *J. Echocardiogr.*, vol. 12, no. 1, pp. 1–11, 2014.

[5] D. Liang, A. Paloma, S. S. Kuppahally, C. Miller, and I. Schnittger, "Multiplanar visualization in 3D transthoracic echocardiography for precise delineation of mitral valve pathology," *Echocardiography*, vol. 25, no. 1, pp. 84–87, 2008.

[6] R. Pini, "Apparatus for obtaining a three-dimensional reconstruction of anatomic structures through the acquisition of echographic images," U.S. Patent 5 159 931, Nov. 3, 1992.

[7] D. P. Shattuck, M. D. Weinshenker, S. W. Smith, and O. T. von Ramm, "Explososcan: A parallel processing technique for high speed ultrasound imaging with linear phased arrays," *J. Acoust. Soc. Amer.*, vol. 75, no. 4, pp. 1273–1282, 1984.

[8] O. T. von Ramm, S. W. Smith, and H. G. Pavy Jr., "High-speed ultrasound volumetric imaging system—Part II: Parallel processing and image display," *IEEE Trans. Ultrason., Ferroelectr., Freq. Control*, vol. 38, no. 2, pp. 109–115, Mar. 1991.

[9] B. Diarra, "Study and optimization of 2D matrix arrays for 3D ultrasound imaging," Ph.D. dissertation, Universit´e Claude Bernard Lyon 1, France, 2014.

[10] S. I. Nikolov and J. A. Jensen, "Application of different spatial sampling patterns for sparse array transducer design," *Ultrasonics*, vol. 37, no. 10, pp. 667–671, 2000.

[11] A. Austeng and S. Holm, "Sparse 2D arrays for 3D phased array imaging-design methods," *IEEE Trans. Ultrason., Ferroelectr., Freq. Control*, vol. 49, no. 8, pp. 1073–1086, Aug. 2002.

[12] B. Diarra, M. Robini, P. Tortoli, C. Cachard, and H. Liebgott, "Design of optimal 2D nongrid sparse arrays for medical ultrasound," *IEEE Trans. Biomed. Eng.*, vol. 60, no. 11, pp. 3093–3102, Nov. 2013.

[13] J. W. Choe *et al.*, "Volumetric real-time imaging using a CMUT ring array," *IEEE Trans. Ultrason., Ferroelectr., Freq. Control*, vol. 59, no. 6, pp. 1201–1211, Jun. 2012.

[14] J. W. Choe, A. Nikoozadeh, Ö. Oralkan, and B. T. Khuri-Yakub, "GPU-based real-time volumetric ultrasound image reconstruction for a ring array," *IEEE Trans. Med. Imag.*, vol. 32, no. 7, pp. 1258–1264, Jul. 2013.

[15] B. Savord and R. Solomon, "Fully sampled matrix transducer for real time 3D ultrasonic imaging," in *Proc. IEEE Symp. Ultrason.*, 2003, vol. 1, pp. 945–953.

[16] S. I. Nikolov and J. A. Jensen, "Investigation of the feasibility of 3D synthetic aperture imaging," in *Proc. IEEE Symp. Ultrason.*, 2003, vol. 2, pp. 1903–1906.

[17] I. O. Wygant, M. Karaman, Ö. Oralkan, and B. T. Khuri-Yakub, "Beamforming and hardware design for a multichannel front-end integrated circuit for real-time 3D catheter-based ultrasonic imaging," in *Proc. Med. Imag.*, 2006, p. 61470A.

[18] M. Yang, R. Sampson, S. Wei, T. F. Wenisch, and C. Chakrabarti, "Separable beamforming for 3D medical ultrasound imaging," *IEEE Trans. Signal Process.*, vol. 63, no. 2, pp. 279–290, Jan. 2015.

[19] K. Owen, M. Fuller, and J. Hossack, "Application of X–Y separable 2D array beamforming for increased frame rate and energy efficiency in handheld devices," *IEEE Trans. Ultrason., Ferroelectr., Freq. Control*, vol. 59, no. 7, pp. 1332–1343, Jul. 2012.

[20] O. Lorintiu, H. Liebgott, M. Alessandrini, O. Bernard, and D. Friboulet, "Compressed sensing reconstruction of 3D ultrasound data using dictionary learning," in *Proc. IEEE Int. Conf. Image Process. (ICIP)*, 2014, pp. 1317–1321.

[21] O. Lorintiu, H. Liebgott, M. Alessandrini, O. Bernard, and D. Friboulet, "Compressed sensing reconstruction of 3D ultrasound data using dictionary learning and line-wise subsampling," *IEEE Trans. Med. Imag.*, vol. 34, no. 12, pp. 2467–2477, Dec. 2015.

[22] Y. C. Eldar, *Sampling Theory: Beyond Bandlimited Systems*. Cambridge, U.K.: Cambridge Univ. Press, 2015.

[23] Y. C. Eldar and G. Kutyniok, *Compressed Sensing: Theory and Applications*. Cambridge, U.K.: Cambridge Univ. Press, 2012.

[24] R. Tur, Y. C. Eldar, and Z. Friedman, "Innovation rate sampling of pulse streams with application to ultrasound imaging," *IEEE Trans. Signal Process.*, vol. 59, no. 4, pp. 1827–1842, Apr. 2011.

[25] X. Zhuang, Y. Zhao, Z. Dai, H. Wang, and L. Wang, "Ultrasonic signal compressive detection with sub-Nyquist sampling rate," *J. Sci. Ind. Res.*, vol. 71, pp. 195–199, 2012.

[26] J. Zhou, Y. He, M. Chirala, B. M. Sadler, and S. Hoyos, "Compressed digital beamformer with asynchronous sampling for ultrasound imaging," in *Proc. IEEE Int. Conf. Acoust. Speech Signal Process. (ICASSP)*, 2013, pp. 1056–1060.

[27] H. Liebgott, R. Prost, and D. Friboulet, "Pre-beamformed RF signal reconstruction in medical ultrasound using compressive sensing," *Ultrasonics*, vol. 53, no. 2, pp. 525–533, 2013.

[28] A. Achim, B. Buxton, G. Tzagkarakis, and P. Tsakalides, "Compressive sensing for ultrasound RF echoes using a-stable distributions," in *Proc. Annu. Int. Conf. IEEE Eng. Med. Biol. Soc. (EMBC)*, 2010, pp. 4304–4307.

[29] G. Tzgkarakis, A. Achim, P. Tsakalides, and J.-L. Starck, "Joint reconstruction of compressively sensed ultrasound RF echoes by exploiting temporal correlations," in *Proc. IEEE 10th Int. Symp. Biomed. Imag. (ISBI)*, 2013, pp. 632–635.

[30] C. Quinsac, A. Basarab, and D. Kouamé, "Frequency domain compressive sampling for ultrasound imaging," *Adv. Acoust. Vibr.*, vol. 2012, pp. 1–16, 2012.

[31] N. Wagner, Y. C. Eldar, and Z. Friedman, "Compressed beamforming in ultrasound imaging," *IEEE Trans. Signal Process.*, vol. 60, no. 9, pp. 4643–4657, Sep. 2012.

[32] T. Chernyakova and Y. C. Eldar, "Fourier domain beamforming: The path to compressed ultrasound imaging," *IEEE Trans. Ultrason., Ferroelectr., Freq. Control*, vol. 61, no. 8, pp. 1252–1267, Aug. 2014.

[33] K. Gedalyahu, R. Tur, and Y. C. Eldar, "Multichannel sampling of pulse streams at the rate of innovation," *IEEE Trans. Signal Process.*, vol. 59, no. 4, pp. 1491–1504, Apr. 2011.

[34] E. Baransky, G. Itzhak, I. Shmuel, N. Wagner, E. Shoshan, and Y. C. Eldar, "Sub-Nyquist radar prototype: Hardware and algorithm," *IEEE Trans. Aerosp. Electron. Syst.*, vol. 50, no. 2, pp. 809–822, Apr. 2014.

[35] V. Murino and A. Trucco, "Underwater 3D imaging by FFT dynamic focusing beamforming," in *Proc. IEEE Int. Conf. Image Process. (ICIP)*, 1994, vol. 1, pp. 890–894.

[36] H. L. Van Trees, *Detection, Estimation, and Modulation Theory, Optimum Array Processing*. New York, NY, USA: Wiley-Interscience, 2004.

[37] S. Becker, J. Bobin, and E. J. Candès, "NESTA: A fast and accurate first-order method for sparse recovery," *SIAM J. Imag. Sci.*, vol. 4, no. 1, pp. 1–39, 2011.

[38] B. E. Treeby and B. T. Cox, "k-Wave: MATLAB toolbox for the simulation and reconstruction of photoacoustic wave fields," *Biomed. Opt.*, vol. 15, no. 2, p. 021314, 2010.

Amir Burshtein received the B.Sc. degree in electrical engineering (*summa cum laude*) and the B.Sc. degree in physics (*summa cum laude*), both from the Technion, Israel Institute of Technology, Haifa, Israel, in 2014. He is currently pursuing the M.Sc. degree in physics with Tel-Aviv University (TAU), Tel-Aviv, Israel.

Michael Birk, photograph and biography not available at the time of publication.

Tanya Chernyakova (S'13) received the B.Sc. degree in biomedical engineering (*cum laude*) from Technion, Israel Institute of Technology, Haifa, Israel, in 2011. She is currently pursuing the Ph.D. degree in electrical engineering at Technion, Israel Institute of Technology. Her research interests include theoretical aspects of signal processing, sampling theory, compressed sensing, medical imaging, and advanced signal processing methods for ultrasonic imaging.

Ms. Chernyakova was an Ollendorff Fellow in 2013 and 2014. She was in the Andrew and Erna Finci Viterbi Fellowship Program in 2016. She was the recipient of the David and Tova Freud and Ruth Freud-Brendel Memorial Scholarship, in 2014.

Alon Eilam received B.Sc. degree in electrical engineering and M.Sc. degree in electrical engineering, both from the Technion, Israel Institute of Technology, Haifa, Israel, in 1982 and 1991, respectively.

His key achievements are development of the world's first digital signal-processor-based chip set for cellular phones with DSP Group Inc., Pioneering Voice over IP technology for the emerging internet with AudioCodes Ltd., and leading the global research and development of WiFi chip sets with Texas Instruments Inc. From 2013 to 2015, he was with Prof. Yonina C. Eldar's group. His research interests are systems engineering, signal processing, and communication.

Arcady Kempinski, photograph and biography not available at the time of publication.

Yonina C. Eldar (S'98–M'02–SM'07–F'12) received the B.Sc. degree in physics in 1995 and the B.Sc. degree in electrical engineering in 1996, both from Tel-Aviv University (TAU), Tel-Aviv, Israel, and the Ph.D. degree in electrical engineering and computer science in 2002 from the Massachusetts Institute of Technology (MIT), Cambridge, MA, USA.

From January 2002 to July 2002, she was a Postdoctoral Fellow at the Digital Signal Processing Group at MIT. She is currently a Professor in the Department of Electrical Engineering at the Technion—Israel Institute of Technology, Haifa, Israel, where she holds the Edwards Chair in Engineering. She is also a Research Affiliate with the Research Laboratory of Electronics at MIT and was a Visiting Professor at Stanford University, Stanford, CA, USA. She is author of the book "Sampling Theory: Beyond Bandlimited Systems" and coauthor of the books "Compressed Sensing" and "Convex Optimization Methods in Signal Processing and Communications," all published by Cambridge University Press. Her research interests are in the broad areas of statistical signal processing, sampling theory and compressed sensing, optimization methods, and their applications to biology and optics.

Dr. Eldar has received numerous awards for excellence in research and teaching, including the IEEE Signal Processing Society Technical Achievement Award (2013), the IEEE/AESS Fred Nathanson Memorial Radar Award (2014), and the IEEE Kiyo Tomiyasu Award (2016). She was a Horev Fellow of the Leaders in Science and Technology program at the Technion and an Alon Fellow. She received the Michael Bruno Memorial Award from the Rothschild Foundation, the Weizmann Prize for Exact Sciences, the Wolf Foundation Krill Prize for Excellence in Scientific Research, the Henry Taub Prize for Excellence in Research (twice), the Hershel Rich Innovation Award (three times), the Award for Women with Distinguished Contributions, the Andre and Bella Meyer Lectureship, the Career Development Chair at the Technion, the Muriel & David Jacknow Award for Excellence in Teaching, and the Technion's Award for Excellence in Teaching (two times). She received several best paper awards and best demo awards together with her research students and colleagues including the SIAM outstanding Paper Prize and the IET Circuits, Devices and Systems Premium Award, and was selected as one of the 50 most influential women in Israel. She is a member of the Young Israel Academy of Science and Humanities and the Israel Committee for Higher Education. She is the Editor-in-Chief of *Foundations and Trends in Signal Processing*, a member of the IEEE Sensor Array and Multichannel Technical Committee, and serves on several other IEEE committees. In the past, she was a Signal Processing Society Distinguished Lecturer, member of the IEEE Signal Processing Theory and Methods and Bio Imaging Signal Processing technical committees, and served as an associate editor for the IEEE Transactions on Signal Processing, the *EURASIP Journal of Signal Processing*, the *SIAM Journal on Matrix Analysis and Applications*, and the *SIAM Journal on Imaging Sciences*. She was Cochair and Technical Cochair of several international conferences and workshops.